Wake meandering statistics of a model wind turbine: Insights gained by large eddy simulations

Daniel Foti, Xiaolei Yang, and Michele Guala
St. Anthony Falls Laboratory, University of Minnesota, Minneapolis, Minnesota 55455, USA

Fotis Sotiropoulos*
Department of Civil Engineering, College of Engineering and Applied Science, Stony Brook University, Stony Brook, New York 11794, USA
(Received 2 March 2016; published 16 August 2016)

Wind tunnel measurements in the wake of an axial flow miniature wind turbine provide evidence of large-scale motions characteristic of wake meandering [Howard *et al.*, Phys. Fluids **27**, 075103 (2015)]. A numerical investigation of the wake, using immersed boundary large eddy simulations able to account for all geometrical details of the model wind turbine, is presented here to elucidate the three-dimensional structure of the wake and the mechanisms controlling near and far wake instabilities. Similar to the findings of Kang *et al.* [Kang *et al.*, J. Fluid Mech. **744**, 376 (2014)], an energetic coherent helical hub vortex is found to form behind the turbine nacelle, which expands radially outward downstream of the turbine and ultimately interacts with the turbine tip shear layer. Starting from the wake meandering filtering used by Howard *et al.*, a three-dimensional spatiotemporal filtering process is developed to reconstruct a three-dimensional meandering profile in the wake of the turbine. The counterwinding hub vortex undergoes a spiral vortex breakdown and the rotational component of the hub vortex persists downstream, contributing to the rotational direction of the wake meandering. Statistical characteristics of the wake meandering profile, along with triple decomposition of the flow field separating the coherent and incoherent turbulent fluctuations, are used to delineate the near and far wake flow structures and their interactions. In the near wake, the nacelle leads to mostly incoherent turbulence, while in the far wake, turbulent coherent structures, especially the azimuthal velocity component, dominate the flow field.

DOI: 10.1103/PhysRevFluids.1.044407

I. INTRODUCTION

The complex dynamics in the wake of a turbine defines the inflow conditions of downstream turbines in a wind power plant and further leads to uncertainty in power output and structural load estimates. Wake meandering, which is described as a low-frequency periodic helical motion in the wake of the wind turbine similar to what occurs in the wake of bluff bodies [1], is an important feature in the turbine's far wake and has been of increased interest to wind energy researchers. Several wind plant studies [2,3] have reported the effects of large-scale flow structures associated with wake meandering on the performance of downstream turbines. These works provided insights into the turbulence levels within the fully developed wind farms and suggested that wake meandering and wake interactions are among the mechanisms contributing to large-scale variability and unsteady loads. Experimental [1], theoretical [4], and computational [5] work has been carried out to investigate the origin of wake meandering. However, few systematic studies on the statistics of wake meandering are available (see, e.g., [6]). This paper is devoted to the investigation of the

*Corresponding author: fotis.sotiropoulos@stonybrook.edu

statistics of wake meanders using the three-dimensional data from a geometry-resolving large eddy simulation (LES) of a model wind turbine.

Medici and Alfredsson [1] first observed in wind tunnel experiments the low-frequency motion in the wake of a wind turbine resembling the vortex shedding from a bluff body and defined it as wake meandering. Further analysis [7] showed that this feature is influenced by the operating conditions of the wind turbine. The low-frequency motion has been detected in other wind tunnel experiments including Chamorro *et al.* [8] and Okulov *et al.* [9]. Immediately downstream of the turbine, helical vortex pairs emerge from the tip and root of each turbine blade as well as a central hub vortex. The vortex structures formed by the tip of the blade, the so-called tip vortices, have been examined extensively both experimentally [10–12] and numerically [5,13,14] and are shown to convect downstream and slowly break down and dissipate partly due to the destabilizing interactions of helical vortices [15–17]. The interaction and stability of the hub vortex and the surrounding tip vortices were examined by Felli *et al.* [18] in a water tunnel using a marine propeller. In ideal conditions, Felli *et al.* [18] found that the hub vortex also becomes destabilized and begins to oscillate at a low frequency, comparable to the propeller rotational frequency, downstream of the tip vortices breakdown. Okulov and Sørensen [4] approached the problem theoretically using stability analysis of the helical tip vortices with a hub vortex model imposed. The study revealed that the stability of the tip vortices depends on the radial extent of the hub vortex and that the entire vortex system is unconditionally unstable. More recently, Okulov *et al.* [9], using a model wind turbine, showed the Strouhal number of the low-frequency motion in the far wake to be constant under several operating conditions. Furthermore, Iungo *et al.* [19] showed that the hub vortex is inherently unstable and it is linked to wake meandering downstream. A recent study investigating an axial flow hydrokinetic turbine by Kang *et al.* [20] further revealed that the interaction of the inner hub vortex with outer tip shear layer plays an important role in triggering the meandering of the far wake. The statistics of wake meandering was recently investigated by Howard *et al.* [6] using the data from a particle image velocimetry (PIV) experiment of a miniature wind turbine. In their study, the instantaneous velocity fields were spatially filtered to track the coherent wake meandering structure as a two-dimensional wave downwind of the turbine. Some interesting dynamics of the wake meandering oscillations were revealed for the wind turbine in several operating conditions. However, the experiments were only able to investigate a two-dimensional flow field, not the three-dimensional nature of the turbine wake. In the present study, we investigate the three-dimensional dynamics of the wake meandering motivated by the work of Howard *et al.* [6]

The actuator line model, which parametrizes the turbine blade as a rotating line, can capture the tip vortices shedding from the blades and has been widely employed in wind turbine and farm simulations. Using the actuator line model, Ivanell *et al.* [5] investigated the instability of tip vortices and its effects on the downwind flow features. Larsen *et al.* [21] employed the computational data from actuator-based models and experimental measurements to develop, calibrate, and validate a dynamic wake meandering model. However, it was found by Kang *et al.* [20] that the actuator disk model and the actuator line model without including the effects of the nacelle cannot accurately capture the interaction between the inner wake and the outer wake for their hydrokinetic turbine. In the present work we employ large eddy simulations with the curvilinear immersed boundary method (the same method employed by Kang *et al.* [20]) to resolve the geometrical details of the same turbine used by Howard *et al.* [6,22] to capture the entire three-dimensional flow field in the wake of the turbine and nacelle. Using the extensive database from the high-fidelity simulations, we investigate the dynamics and statistics of the three-dimensional coherent helical wake meandering structure reconstructed using a spatiotemporal filtering method.

The paper is organized as follows. Sections II and III explain the immersed boundary large eddy simulation numerical methods and procedure, respectively. The present numerical results are compared with experimental measurements and analyzed in Sec. IV, which includes details of the filtering procedure and discussion of the flow field in terms of the wake meandering reconstruction. The study is summarized in Sec. V.

II. NUMERICAL METHODS

In the same manner as Kang *et al.* [20], we employ LES with the curvilinear immersed boundary method [23] coupled with a wall model for reconstructing the velocity boundary conditions at the immersed boundary nodes. This method has been shown to be an effective robust method for a variety of complex turbulent geophysical flows such as meandering streams [24,25], hydrokinetic turbines in channels [20], and sediment transport in an open channel [26]. Most importantly, this method is capable of resolving the geometry of an axial flow hydrokinetic turbine such as the intricacies of turbine blades, nacelle, and tower with accuracy that deficiencies of actuator based models are indicated quite readily [20].

In our code, the LES is carried by solving the three-dimensional, incompressible, filtered continuity and momentum conservation equations in three-dimensional generalized curvilinear coordinates [27] with a hybrid staggered-nonstaggered grid formulation [28], which in curvilinear coordinates in compact tensor notation (repeated indices imply summation) are as follows ($i, j = 1,2,3$):

$$J\frac{\partial U^i}{\partial \xi^i} = 0, \tag{1}$$

$$\frac{1}{J}\frac{\partial U^i}{\partial t} = \frac{\xi_l^i}{J}\left[-\frac{\partial}{\partial \xi^j}(U^j u_l) + \frac{\mu}{\rho}\frac{\partial}{\partial \xi^j}\left(\frac{g^{jk}}{J}\frac{\partial u_l}{\partial \xi^k}\right) - \frac{1}{\rho}\frac{\partial}{\partial \xi^j}\left(\frac{\xi_l^j p}{J}\right) - \frac{1}{\rho}\frac{\partial \tau_{lj}}{\partial \xi^j}\right], \tag{2}$$

where $\xi_l^i = \partial \xi^i / \partial x_l$ are the transformation metrics, J is the Jacobian of the geometric transformation, u_i is the ith component of the velocity vector in Cartesian coordinates, $U^i = (\xi_m^i / J)u_m$ is the contravariant volume flux, $g^{jk} = \xi_l^j \xi_l^k$ are the components of the contravariant metric tensor, ρ is the density, μ is the dynamic viscosity, p is the pressure, and τ_{ij} represents the anisotropic part of the subgrid-scale stress tensor. The closure for τ_{ij} is provided by a dynamic Smagorinsky model [29] developed by Germano *et al.* [30],

$$\tau_{ij} - \tfrac{1}{3}\tau_{kk}\delta_{ij} = -2\mu_t \tilde{S}_{ij}, \tag{3}$$

where the tilde denotes the grid filtering operation and $\tilde{S}_{ij}$ is the filtered strain-rate tensor. The eddy viscosity μ_t is given by

$$\mu_t = \rho C_s \Delta^2 |\tilde{S}|, \tag{4}$$

where C_s is the dynamically calculated Smagorinsky constant [30], Δ is the filter size taken as the cubic root of the cell volume, and $|\tilde{S}| = (2\tilde{S}_{ij}\tilde{S}_{ij})^{1/2}$. A wall model is used to reconstruct boundary conditions at the immersed boundary nodes as described in detail by Kang *et al.* [23]. The governing equations are discretized with three-point central finite differencing on a hybrid staggered-nonstaggered grid and integrating in time using an efficient fractional step method. For details, see [20,23].

III. TEST CASE SETUP

The simulations are designed after the experiments performed in Ref. [6]. The experiments are conducted in the St. Anthony Falls Laboratory wind tunnel at University of Minnesota. The fixed-pitch three-blade GWS/EP-5030 × 3 rotor has a diameter $D = 0.128$ m at a hub height $H = 0.104$ m. In the experiments, a voltage is applied to maintain a constant tip speed ratio λ. While a few rotational speeds were tested in the experiments, in the present study only the optimal tip speed ratio $\lambda = 3.2$ is simulated. The turbulent boundary layer developed in the wind tunnel has a hub velocity $U_{\text{hub}} = 5\ \text{ms}^{-1}$, a shear velocity $u_\tau = 0.23\ \text{ms}^{-1}$, and an approximate boundary layer height $\delta = 0.6$ m, leading to a Reynolds number based on the turbine diameter $\text{Re}_D = U_{\text{hub}} D/\nu = 42\,977$.

The computational domains used for simulations extends $5D \times 4.69D \times 12D$ in the transverse, vertical, and streamwise directions. The bottom wall is modeled with a wall model [31]. The free-slip

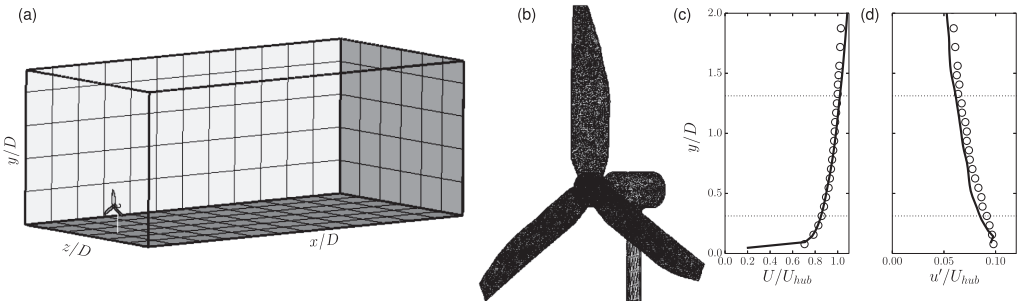

FIG. 1. (a) Computational domain with the wind turbine inside. (b) Wind turbine surface discretized into an unstructured triangular mesh. Inflow (c) mean streamwise velocity and (d) rms streamwise velocity of the experimental measurements of the wind tunnel (circles) and precursory simulation (line).

boundary condition is applied at the top and side walls. The inflow is a fully developed turbulent boundary layer, which is generated from a precursory simulation. The precursory simulation is carried out to replicate the wind tunnel environment with the same Re_D and $\mathrm{Re}_\tau = u_\tau \delta/\nu$ in a domain of size $9D \times 4.69D \times 23D$ to generate a fully developed turbulent boundary layer using periodic boundary conditions along the streamwise and spanwise directions. After sufficient time to allow the flow field to become fully developed, the streamwise mean and rms velocities of the precursory simulation shown in Figs. 1(c) and 1(d), respectively, converge to the experimental estimates. Subsequently, a sufficiently large sample of instantaneous flow fields is saved and fed as inflow conditions for the wind turbine simulations.

Three computational grids are used for the wind turbine study: grid I, grid II, and grid III. These correspond to 8×10^6, 80×10^6, and 110×10^6 grid points, respectively. Further information about the grids can be found in Table I. The grid is stretched such that in the rotor plane extending D downwind, a uniform grid is present with 50, 100, and 150 cells per D in each direction, respectively, for each grid. We continue the simulation for 90 rotor rotations, which is found adequate to obtain statistically converged flow fields. A grid sensitivity study was performed, shown in Fig. 2, with grid III providing the best results comparable to the experiments. As such, all results shown here use the data from grid III unless otherwise specified.

The wind turbine geometry including blade, nacelle, and tower is discretized with an unstructured triangular mesh shown in Fig. 1. The twist of the blades are described in Ref. [22]. Because of the very thin turbine model blades and because we do not have the information of the specific airfoil type, in this simulation, the blades are modeled as a twisted pitched flat plat with zero thickness. The thin blade implementation prescribes the boundary conditions on the upwind and downwind surfaces of the blades but without having structure nodes present between the surfaces [32].

IV. RESULTS AND DISCUSSION

In this section, first, the results of the large eddy simulation of the wind turbine will be compared with experimental measurements and discussed. Then the wake meandering filter technique used by

TABLE I. Grid size and resolution domains used for LES.

Grid	Total cells	Cells per D
grid I	$150 \times 130 \times 550$	50
grid II	$300 \times 260 \times 1000$	100
grid III	$350 \times 290 \times 1050$	150

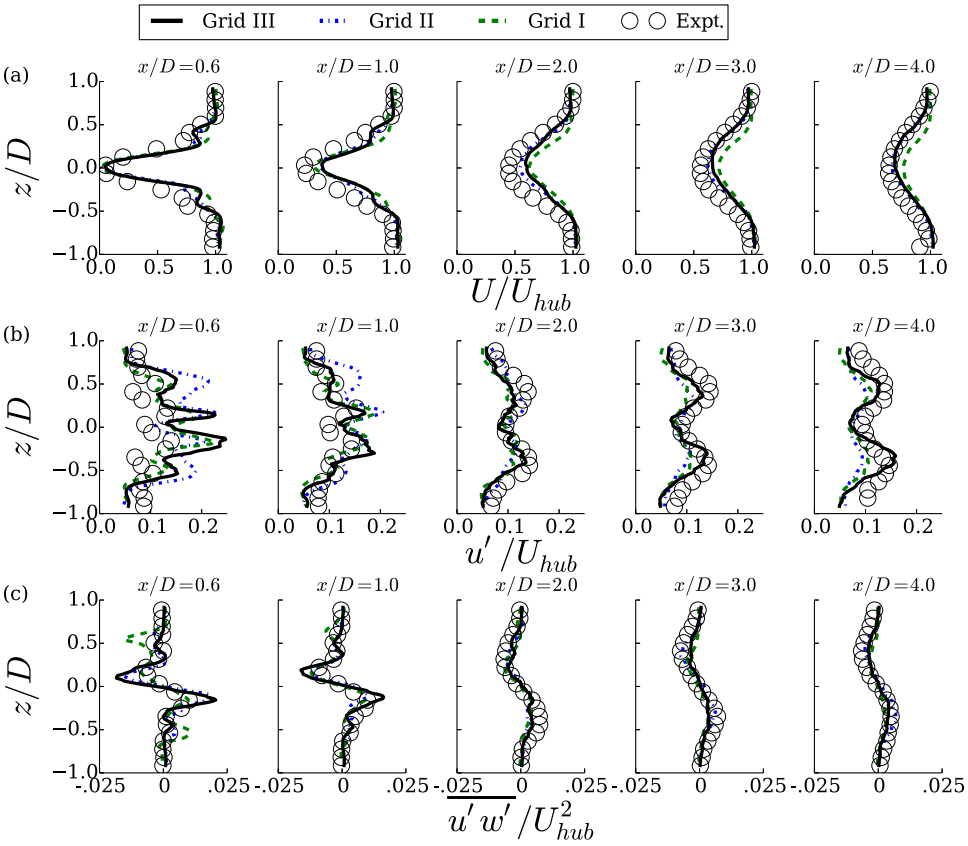

FIG. 2. Comparison between PIV measurements and LES of time-averaged flow statistics: (a) U/U_{hub}, (b) u'/U_{hub}, and (c) $\overline{u'w'}/U_{\text{hub}}^2$ at the hub height $y = 0.8125D$. The profiles are shown at axial distances $x/D = 0.55, 1.0, 2.0, 3.0, 4.0$ from the rotor plane.

Howard *et al.* [6] will be further developed for the use in three-dimensional large eddy simulation results. Finally, a spatial and temporal statistical analysis of the filtered wake meandering profile will be discussed.

A. Validation of the computed results

Figure 2(a) shows the comparison of the mean streamwise velocity U LES results of grids I, II, and III with the experimental PIV observations at several locations downstream of the wind turbine. First, as the number of grid points increases in the simulation, the results trend towards the experimental results in all locations. In particular, grid III is able to provide a more accurate flow description close to the turbine between the wake from the nacelle (inner wake) and the wake from the turbine rotor (outer wake) as shown in the velocity step change near spanwise location $z/D = \pm 0.25$ at $x/D = 0.5$ and $x/D = 1$. There is only a slight discrepancy in the first profile because of the differences between the modeled and actual blade geometries. Farther downstream $x/D > 2$, the inner and outer features merge, the velocity step disappears, and the measurements of the mean velocity profile tend to collapse with the numerical results. Both experimental and simulation results display a slight asymmetry in the profiles due to the rotation of the turbine. The rms of the streamwise velocity u' and spanwise-streamwise $\overline{u'w'}$ correlation are shown in Figs. 2(b) and 2(c), respectively. With these quantities, only grid III is able to give accurate results in comparison to the experiments. The shear layers in the nacelle wake and the rotor wake are well captured but are overpredicted by

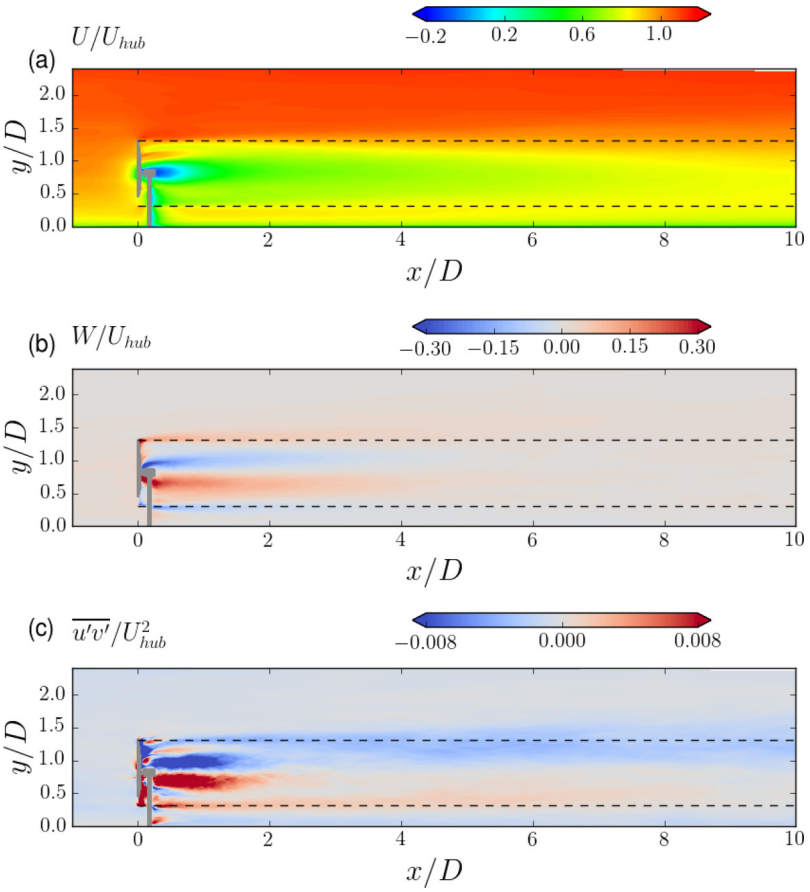

FIG. 3. Contours of the time-averaged flow statistics for (a) U/U_{hub}, (b) W/U_{hub}, and (c) $\overline{u'v'}/U_{\text{hub}}^2$ at the $z/D = 0$ plane. The dashed lines indicate the maximum and minimum vertical heights of the blade tip.

the simulations. This indicates that the discretization of the turbine blades as a flat plate may have some effects on the turbulence close to the turbine. However, in the simulated shear layers, the peaks of both u' and $\overline{u'w'}$ decrease to the corresponding levels measured in the experiments by $x/D = 1$. In both the experiments and simulations, the two shear layers merge into one shear layer with a maximum near the rotor tip by $x/D = 2$. Profiles farther downstream have a slight discrepancy of no more that 5% in the shear layers peaks, which indicates that further grid refinement or time averaging may be necessary. Nevertheless, the simulations with modeling the blades as flat plates appear to adequately predict the flow field of the miniature wind turbine.

The contours of the time-averaged mean and turbulent statistics are shown in Fig. 3 at the centerline plane $z = 0$. The spatial distribution of the mean streamwise velocity U/U_{hub} is shown in Fig. 3(a) by plotting velocity contours. The streamwise momentum deficit is clearly present and shown to slowly recover downstream. Within $x/D = 0.5$, the wake is comprised of an inner flow recirculation zone with a minimum of $U/U_{\text{hub}} \sim -0.2$ and an outer region with positive streamwise velocity expanding towards the outer boundary of the wake defined by the tip vortices. For further downstream locations, the wake is mainly dominated by the region with positive streamwise velocity. The mean spanwise velocity W/U_{hub} in Fig. 3(b) indicates that close to the turbine two counterrotating wakes exist: (i) The inner wake has counterwinding rotation compared to the turbine blades, which is the footprint of the time-averaged rotation of the hub vortex, and (ii) the outer wake is present as the footprint of the tip vortices and corotates with the turbine blades. A similar pattern consisting of two counterrotating

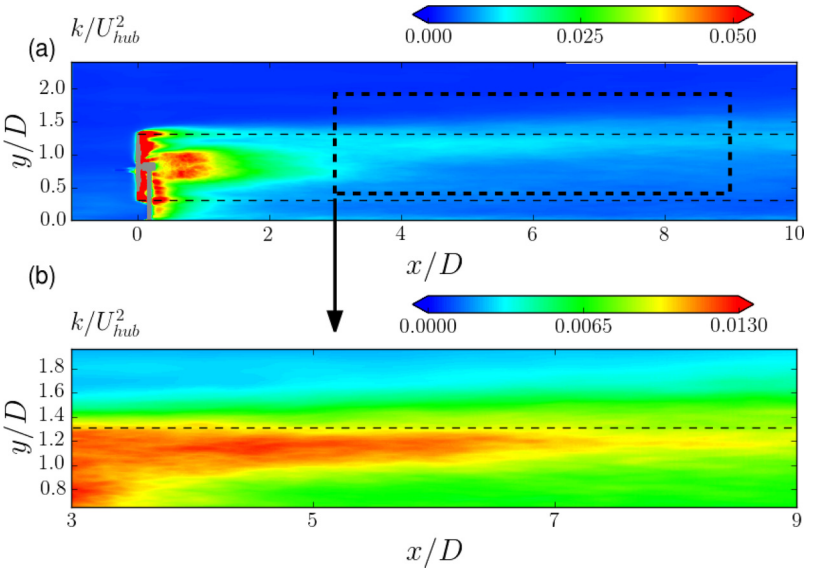

FIG. 4. Contours of the turbulence kinetic energy k/U_{hub}^2 at the $z/D = 0$ plane. The boxed area in (a) is magnified in (b) to show the extent of the top-tip k/U_{hub}^2 contours. The fine dashed lines indicate the maximum and minimum vertical heights of the blade tip.

regions in the wake was also seen in the hydrokinetic turbine simulation of Kang *et al.* [20] and the experimental results of Chamorro *et al.* [8] and is consistent with the Joukowski turbine wake model [33], which proposes, for an N-blade turbine, N helical tip vortices and a counterrotating hub vortex. The rotations of the inner wake and the outer wake remain distinct features for a few diameters downstream until interactions between the outwardly expanding inner wake and the outer wake merge near the tip position at about $x/D = 4$. The mean azimuthal momentum becomes negligible for both wakes within $x/D = 5$. In Fig. 3(c) the Reynolds shear stress $\overline{u'v'}/U_{\text{hub}}^2$ is intense in the near wake region in specific locations where the hub vortex and the tip vortices are concentrated. Along the blade, high shear stress regions exist from the root of the blade to the tip, where the blade vortex is located or where the unsteadiness associated with the blade passing is expected to occur. Behind the nacelle, two regions of high and low mean turbulence shear stress extending to $x/D = 3$ and merging with turbulence shear stress contributions along the top and bottom tip positions identify the high turbulence mixing occurring in the shear layer of the inner wake. The turbulence shear stress at the tips delineates regions across which steep velocity gradients increase and large turbulence mixing occurs. This is particularly important along the top tip shear layer, where high turbulence kinetic energy extends past $x/D = 4$.

The turbulence kinetic energy (TKE) k/U_{hub}^2 is shown in Fig. 4. Near the turbine the TKE is high in the shear layers of the inner wake and the tip vortices formed at the tip of the blades. As the shear layers expand downwind, the TKE decreases and spreads with the shear layers around the hub vortex in nearly parallel streaks. The TKE exists in the shear layers of the inner wake and in the vicinity of the hub vortex. The high levels of nacelle and hub vortex TKE extend $3D$ downstream and merge with the high TKE along the top tip position. Regions of higher levels of k/U_{hub}^2 exist above and below the nacelle in the shear layers of the inner wake. At $4D$ downstream, the TKE increases again in the top-tip shear layer, similar to the findings in Kang *et al.* [20]. Figure 4(b) magnifies the region around the top-tip shear layer and shows how k/U_{hub}^2 increases, peaks around $x/D = 5$, and extends farther downstream the top-tip position. The increased turbulence in the far wake, around the outer shear layer, marks the interaction of hub and tip shear layers, inner and outer wakes, and the onset of large-scale wake meandering. The TKE near the bottom-tip shear layer is less pronounced mainly due to the significantly lower incoming wind speed.

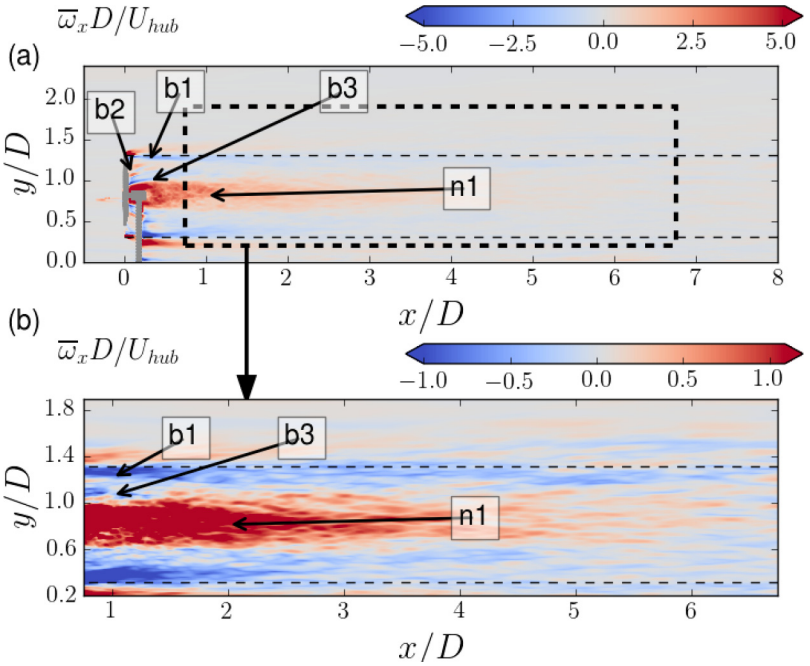

FIG. 5. Contours of the time-averaged streamwise vorticity $\overline{\omega_x} D/U_{\text{hub}}$ at the $z/D = 0$ plane. The boxed area in (a) is magnified in (b). The fine dashed lines indicate the maximum and minimum vertical heights of the blade tip.

The time-averaged streamwise vorticity $\omega_x D/U_h$ contours, shown in Fig. 5, reveal a number of shear regions with high vorticity in the near-turbine wake that originate from both the blades and nacelle. Along the blade, several vortex structures are created and marked on Fig. 5: tip vortices ($b1$), weak midplane blade vortices ($b2$), and root vortices ($b3$) produced near the root of the blades with the center hub. The tip vorticity remains concentrated along the top-tip position for many diameters downstream, slowly dissipating as the shear layer formed by the tip vortices expands. Along the bottom-tip position the footprint of the tip vortices can be seen directly after the blade tip and appears to interact with the turbine tower. The interaction imparts a consistent stronger pair of vortices that continues downstream along the bottom-tip position. The midplane blade vortices form from the trailing edge of the blades and quickly dissipate. The root vortices form a V-shaped contour (in fact, a conical shape in three dimensions) and extend downstream enclosing a hub vortex core ($n1$) formed behind the nacelle. The root vortices mark the exterior boundary of the inner wake and radially expand outward towards the tip position. The root vorticity merges with the tip vorticity at $x/D = 1$ and the hub vortex core continues to expand and interact with the tip vortices. Between $2 < x/D < 5$ downwind, the expanding hub vortex interacts with the tip vortices shown clearly in Fig. 5(b) and begins to dissipate while remaining persistent far into the wake flow field. Vorticity along the top-tip position persists farther downstream, consistent with the spatial evolution of the turbulence kinetic energy. The mean flow field shows clearly the footprint of the hub vortex, tip vortices, and wake meandering. In the following sections, further evidence of the importance of these features and analysis of instantaneous flow fields is developed to understand the physical mechanisms of these features.

B. Wake meandering filtering technique

From the LES, instantaneous snapshots of the velocity field are collected with a time step $\tau_s = T/770$, where T is the period of one revolution of the turbine rotor. This temporal resolution,

along with the spatial resolution of grid III, allow us to investigate the evolution of wake meandering. Wake meandering presents itself downwind of the turbine as a large coherent structure. While its presence has been hypothesized to be related to the bluff body sheddinglike mechanism of the turbine rotor [7] and amplified by the hub vortex [6,20], the wake meandering phenomenon is still not completely understood.

In the present work the structure of a meandering profile through the wake of the wind turbine is reconstructed to investigate the statistics of the meandering fluctuations and understand their physical nature. From the triple decomposition of a turbulent flow [34]

$$\boldsymbol{u}(\boldsymbol{x},t) = \boldsymbol{U}(\boldsymbol{x}) + \tilde{\boldsymbol{u}}(\boldsymbol{x},t) + \boldsymbol{u_i}(\boldsymbol{x},t). \tag{5}$$

The instantaneous velocity vector $\boldsymbol{u}(\boldsymbol{x},t)$ (bold indicates a vector quantity) can be decomposed into a strictly spatial mean term $\boldsymbol{U}(\boldsymbol{x})$, a coherent term $\tilde{\boldsymbol{u}}(\boldsymbol{x},t)$, and the incoherent term $\boldsymbol{u_i}(\boldsymbol{x},t)$. Alternatively,

$$\boldsymbol{u}(\boldsymbol{x},t) = \langle \boldsymbol{u} \rangle(\boldsymbol{x},t) + \boldsymbol{u_i}(\boldsymbol{x},t). \tag{6}$$

The mean velocity $\boldsymbol{U}(\boldsymbol{x})$ and coherent velocity $\tilde{\boldsymbol{u}}(\boldsymbol{x},t)$ can be summed as a large-scale velocity $\langle \boldsymbol{u} \rangle(\boldsymbol{x},t)$ of the coherent structure.

In the following analysis we attempt to derive a robust technique to identify the coherent structure corresponding to wake meandering. As in Ref. [6], large-scale coherent meandering profiles are instantaneously reconstructed from the velocity minima in the streamwise direction. Howard *et al.* [6], however, reconstructed two-dimensional wake meandering profiles since experimental data were only available on two-dimensional planes. Here we take advantage of the LES flow fields to develop an approach for reconstructing the three-dimensional (3D) wake meandering profiles. To do so we first determine the coherence time and length scales of wake meandering. Subsequently, we employ the so-determined scales to temporally and spatially filter the instantaneous flow fields to better visualize the coherent wake dynamics. A two-part filtering technique is employed.

To determine the coherence time scale of meandering we employ two different approaches. The first approach is based on the fluctuation analysis proposed by Chrisohoides and Sotiropoulos [35] to identify the coherence time scale of the energetic coherent structures in experimental visualizations of complex free-surface flows. We begin by applying a finite time averaging of the instantaneous flow field over a finite size window τ as follows:

$$u_\tau(x,t) = \frac{1}{\tau} \int_{t-\tau/2}^{t+\tau/2} u(x,t')dt'. \tag{7}$$

According to the Chrisohoides-Sotiropoulos approach [35], the coherence time scale τ_c of wake meandering is the optimal size of a finite-size temporal averaging window τ based on statistical evidence using the central-limit theorem and fluctuation analysis. If the temporal averaging window is too short, the finite time averaged time series resulting from Eq. (7) will still be dominated by incoherent motions. If the window is too long, on the other hand, the energetic coherent motions are completely smeared out. To find the optimal coherence time scale τ_c, we employ fluctuation analysis as proposed by Chrisohoides and Sotiropoulos [35]. For a given finite time averaging window τ, the standard deviation of the time series E_τ is calculated as follows:

$$[E_\tau(x)]^2 = \lim_{T\to\infty} \frac{1}{T} \int_0^T [u_\tau(x,t') - U(x)]^2 dt'. \tag{8}$$

From the central-limit theorem, as the temporal averaging window τ is increased, adjacent windows become uncorrelated and E_τ scales as $\tau^{-1/2}$. The coherence time scale is chosen as the time scale for which E_τ just begins to scale as $\tau^{-1/2}$. In Fig. 6(a) we plot $X_\tau = \tau^{1/2} E_\tau$ versus τ for the velocity time series at $x/D = 4$ at the centerline. It is evident from this figure that X_τ becomes flat as the window averaging size τ is increased. We define the coherence time scale of wake meandering as the time step size where the flattening starts, which is found to be $\tau_c = 0.63T$.

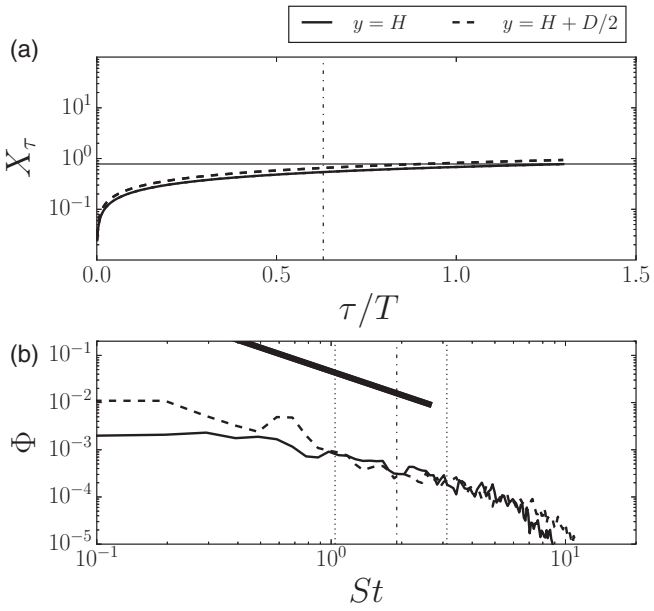

FIG. 6. (a) Fluctuation analysis diagram and (b) velocity energy spectrum along the centerline and top-tip position of the turbine at $x/D = 4$. The thick blade line has a slope of $-5/3$. The thin dashed lines are the turbine frequency and blade frequency. The dash-dotted line marks the determine coherence (a) time scale τ_c and (b) frequency $1/\tau_c$.

The second approach to determine the coherence time scale is to employ spectral analysis. Figure 6(b) shows the energy spectrum for the velocity series at $x/D = 4$ at the centerline with the coherence frequency $1/\tau_c$ also indicated by a dash-dotted vertical line. As can be seen in this figure, the so-determined time scale τ_c is very close to that determined by the fluctuation analysis. Both approaches use a different analysis to separate the short time scales from the time scales of the large coherent structures and both are in good agreement. Using Taylor's frozen turbulence hypothesis along with the so-determined time scale τ_c and the mean centerline velocity at $x/D = 4$, the coherence length scale l_c is approximately equal to $0.5D$. Approximately, the same value is computed when we apply the above analysis to several streamwise locations along the wake. For that we determine $l_c = 0.5D$ to be the characteristic length scale for wake meandering.

After applying the finite time averaging to the full 3D flow field, we attempt to identify the large-scale wake meandering by reconstructing a 3D meandering profile on the velocity minima in the wake of the turbine. The velocity minima are considered the points of minimum instantaneous streamwise velocity in the y-z direction for each x location. First used in the work of Howard *et al.* [6], low-pass spatial filtering uses a cutoff length scale of $0.5D$ (very similar to the coherent time scale presented above) to create a continuous smooth 3D profile.

The procedure used to reconstruct the coherent meander profile is the following. (1) Use finite time averaging to temporally filter the instantaneous data. (2) Find the velocity minima. (3) Spatially filter the velocity minima location points to obtain the filtered 3D meander profile.

The procedure is applied to three-dimensional instantaneous data over a total time $t_{\text{tot}} = 90T$. To elucidate and qualitatively describe the helical shape of the filtered wake meander, several 3D instantaneous views are shown in Fig. 7, captured at four time instances separated by $\Delta t = T/2$. In each instance the helical nature of the meander is evident and further emphasized by the large-scale azimuthal velocity provided for selected planes.

An example of the meander profile at one instance is shown in Fig. 8 with projection of the three-dimensional profile on a side view and a top view plane. In Fig. 8 the velocity minima are

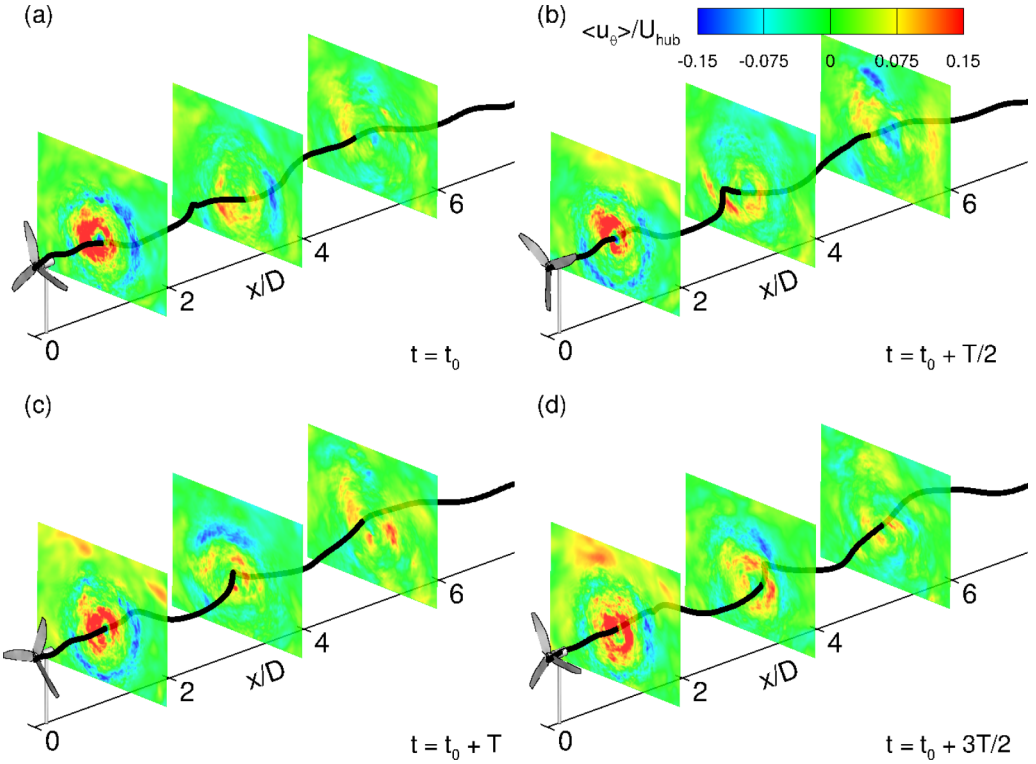

FIG. 7. Four different time instances showing the three-dimensional filtered meander line with azimuthal velocity contours on slices at $x/D = 1,3,5$. The four instances shown are (a) $t = t_0$, (b) $t = t_0 + T/2$, (c) $t = t_0 + T$, and (d) $t = t_0 + 3T/2$.

designated by the circles, while the filtered meander profile is the solid line. The smooth profile, due in part to the spatial filtering, follows the velocity minimum locations; moreover, it tracks the large-scale features present in the velocity contours. From the top view, the meander is biased towards the side of the rotor centerline corresponding to the direction of the rotation of the turbine. However, the vertical extent of the meandering oscillation domain remains mostly below the location of the top tip. The wavelike structure present in each view is reminiscent of the two-dimensional meander identified by Howard *et al.* [6]; indeed, the blue dashed line is a two-dimensional profile using only the in-plane velocity deficit. Qualitatively, from both Figs. 7 and 8, two approximate regions of the meander can be parsed from the behavior indicated by the amplitude and pitch of the helix structure.

(i) *Near field wake*. Immediately after the turbine to around $x/D = 2$ the difference in velocity minimum locations and filtered meander profile is relatively small and the probability of the amplitude of the wave to remain inside the inner wake generated off the nacelle is very high. About two complete wavelengths are present in this region. From the streamwise vorticity contour in Fig. 8(c) we see that the meander profile location closely correlates with the hub vortex.

(ii) *Far wake*. Located at $x/D > 5$, following the large coherent features present in the streamwise velocity contour, the pitch of the meander helix has increased considerably with a high amplitude and interacts outside the radial extent of the turbine blades. Between the near and far wake region, approximately $2 < x/D < 4$, the amplitude increases rapidly such that radially, the meander approaches the tip vortices located at $r/D = \pm 1/2$.

C. Large-scale features and wake meandering profile

We now turn our attention to the details of 3D flow fields and vortical structures associated with the wake meandering profiles. A single time instance of the large-scale azimuthal velocity $\langle u_\theta \rangle$ defined

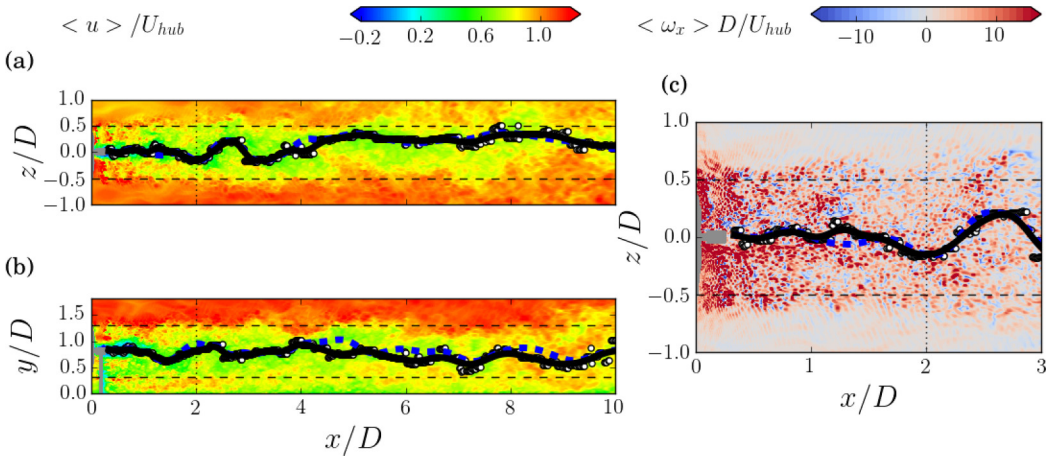

FIG. 8. Time instance of wake meandering profile showing the contours at the (a) hub height plane $y/D = 0.8125$ and (b) centerline plane $z/D = 0$ of the large-scale streamwise velocity $\langle u \rangle$. (c) Hub height plane $y/D = 0.8125$ of large-scale streamwise vorticity $\langle \omega_x \rangle$ overlaid with the positions of the streamwise velocity minima at each axial location, the three-dimensional filtered meander profile projected on the plane, and the two-dimensional filtered meander profile represented by the circle markers, black solid line, and blue dashed line, respectively. The small horizontal dashed lines indicate the blade tip positions. The thin vertical dotted line marks $x/D = 2$.

in Eq. (6) and two-dimensional streamlines associated with the large-scale velocity field are shown in Fig. 9(a) at six different cross sections (constant x) at various locations downstream of the turbine. In each cross-sectional slice, a large red X marks the instantaneous location of the meander profile in the cross section. The large-scale azimuthal velocity has a center red region of counterrotating flow and a thin blue region with corotating flow from $0.5 < x/D < 2$. The streamlines in those cross sections have a spiral sinklike flow suggestive of the hub vortex in the counterrotating region. The center of the spiral sink flow is not axisymmetric and can be seen to move from the center to the left to the right of the turbine hub through the three cross sections of $0.5 < x/D < 2$, while the meander profile intersects the cross section near the center of the sink. Together with Fig. 8(c), this suggests that in the near wake the filtered meander profile follows the hub vortex. In cross sections $x/D \geqslant 4$, the coherence of the hub vortex is broken down, but unlike the mean azimuthal velocity U_θ, the large-scale azimuthal velocity $\langle u_\theta \rangle$ persists farther downstream. This signifies that there is a strong coherent velocity component present in the wake meandering at $x/D \geqslant 4$ that is periodic and thus averages to a negligible mean azimuthal velocity.

Figure 9(b) shows the two-dimensional streamlines of the mean flow with the mean azimuthal velocity U_θ at the same x/D locations as Fig. 9(a). First, appearing at $x/D = 0.5$, the center red region is the counterrotating hub vortex region, while the thin blue region near the turbine tip is the corotating layer representing the footprint of the tip vortices. The overall inner and outer counterrotating shear layer structure observed in this figure is very similar to that found in the simulations of Kang *et al.* [20] and the experiments of Chamorro *et al.* [8] for an axial flow hydrokinetic turbine. The next five cross sections downstream clearly show the rapid decay of the rotational velocities in both the inner and outer two regions up to $x/D = 4$, where the mean rotational velocity becomes negligible. In the near wake at $x/D = 0.5$, the streamlines are nearly axisymmetric. Outside the hub region, the streamlines indicate radial outward expansion through the tip vortices region, which marks the turbine wake expansion. A localized region of rotation also exists along the bottom of the wake, imparted by the interaction of the tip vortices and the tower. This localized region of tower-wake interaction is also witnessed in the streamwise vorticity contours of Fig. 5. It is also evident from Fig. 9(a) that the axisymmetry of the rotating wake begins

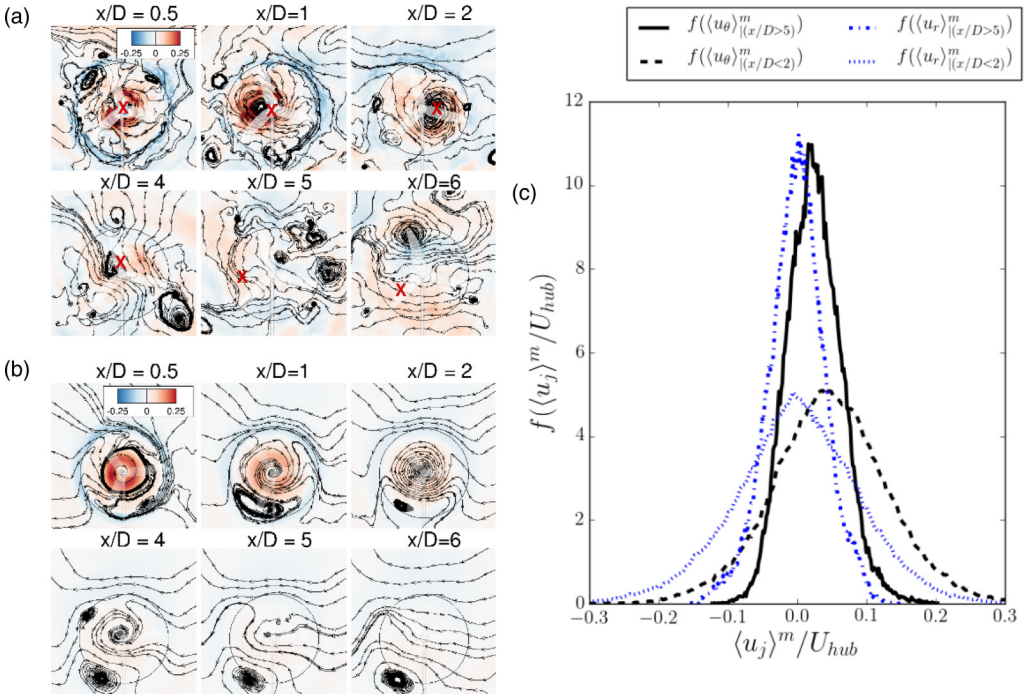

FIG. 9. Contours of (a) large-scale velocity $\langle u_\theta \rangle$ and two-dimensional streamlines and (b) mean azimuthal velocity U_θ and two-dimensional streamlines on six different constant x cross sections downstream of the turbine. (c) Normalized probability density function of large-scale velocity $f(\langle u_j \rangle)$ in the near wake $x/D < 2$ and in the far wake $x/D > 5$.

to break down rapidly in the outer flow region, while the hub region continues to exhibit spiral-like entrainment through $x/D = 4$.

In Fig. 9(c) probability density functions (PDFs) conditioned on the downstream distance in bins for the near wake ($x/D < 2$) and far wake ($x/D > 5$) are shown for the large-scale azimuthal and radial velocities along the meander profiles. It is noted that variables denoted by a superscript m indicate a conditional sampling of the flow field locations that lie along the meander profile. In the near wake, the peak of the azimuthal velocity PDF is positive with a long tail towards higher positive azimuthal velocities that compares well with both the azimuthal velocities in Figs. 9(a) and 9(b), suggesting that the counterrotating center hub region overlaps with the meander profile. The peak probability of the radial velocity is slightly negative because of the entrainment of fluid that occurs in the hub vortex and the meander. The PDF of the azimuthal and radial velocity in the far wake is quite narrow and symmetric and a peak near zero as the mean azimuthal velocity is shown to be negligible in the far wake. Moreover, little correlation is shown with the azimuthal velocity and the meander location because both the positive and negative tails of the distribution are relatively similar. Nonetheless, the azimuthal velocity PDF is slightly shifted positive, suggesting that the rotational momentum of the hub vortex persists downstream into the wake meandering region.

To further understand the three dimensionality of the near wake structures behind the turbine nacelle, isosurfaces of the large-scale streamwise $\langle u \rangle$ and azimuthal $\langle u_\theta \rangle$ velocities are depicted in Fig. 10. Previous evidence from Fig. 9 reflects that the instantaneous hub vortex is asymmetric and the meander profile traces through the hub vortex in the near wake. In addition, Fig. 3(a) indicates a region of mean negative velocity directly behind the nacelle. The isosurface of the large-scale streamwise velocity $\langle u \rangle = 0$ envelops the nacelle starting directly behind the hub of the blades and persists to about $x/D = 0.5$. From the contours and streamlines shown in Fig. 9(b), this region

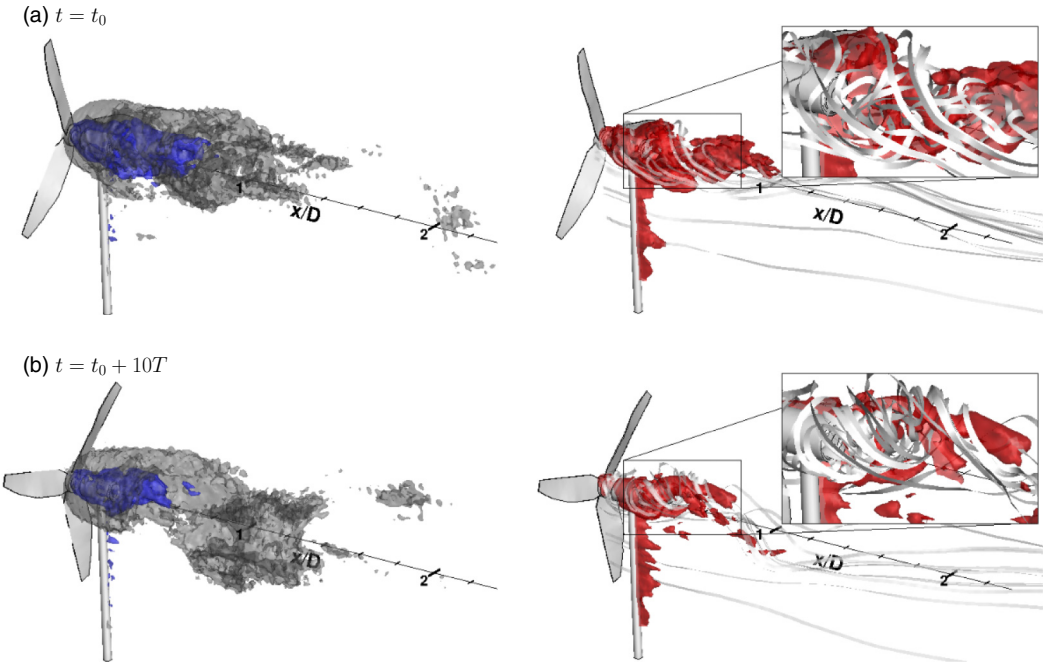

FIG. 10. Isosurfaces of $\langle u_\theta \rangle / U_{\text{hub}} = 0.2$ (dark gray), $\langle u \rangle / U_{\text{hub}} = 0$ (blue), $\langle |u| \rangle / U_{\text{hub}} = 0.2$ (red) with streamlines at two time instances.

reversed flow rotates in the direction opposite to the turbine. It is evident in Fig. 10 that the hub vortex develops a large-scale spiral instability precessing in the direction opposite to the turbine rotation, as was also observed by Kang *et al.* [20] Furthermore, the instantaneous streamlines reveal a structure with a separation bubble emanating from the nacelle of the turbine with a spiral precessing tail, very much reminiscent of the classical vortex breakdown instability [36,37]. The zoomed-in frame of the streamlines and velocity magnitude shows the three-dimensional internal view of the hub vortex with a centerline reversal and toroidal recirculation downstream of the nacelle. The isosurface of the large-scale azimuthal velocity $\langle u_\theta \rangle / U_{\text{hub}} = 0.2$ forms a helical surface that envelopes the flow reversal region with positive azimuthal velocity region extending to $x/D = 2$. The helical meander profiles shown in Fig. 7 before are found to follow closely and in fact arise from the precession of the unstable hub vortex. The region within which the hub vortex precesses is found to continually entrain fluid and expand radially with downstream distance while the meander profile quickly increases in amplitude. With this expansion, the hub vortex begins to interact with the tip shear layer especially at $x/D > 4$, where the previously shown turbulent kinetic energy in Fig. 4 increases, becoming a major contributor to the increased turbulence and wake meandering that emerges in the far wake. These results are essentially identical to the general trends reported by Kang *et al.* [20] for an entirely different turbine design and similar to marine propellers. The helical hub vortex in marine propellers has been studied extensively [18,38,39] and has been shown to rotate counter to the rotation of the propeller. The marine propeller hub vortex has a dominant frequency equal to the rotational frequency of the propeller unlike the wind turbine hub vortex, which has a dominant frequency that less is than the rotational frequency of the turbine rotor. The marine propeller hub vortex advances farther downstream before breakdown as compared to the current model wind turbine partly due to different inflow (wind turbine is situated in a boundary layer). In marine hydrokinetic turbines, especially the one presented in Ref. [20], the hub vortex behaves similarly to the present results.

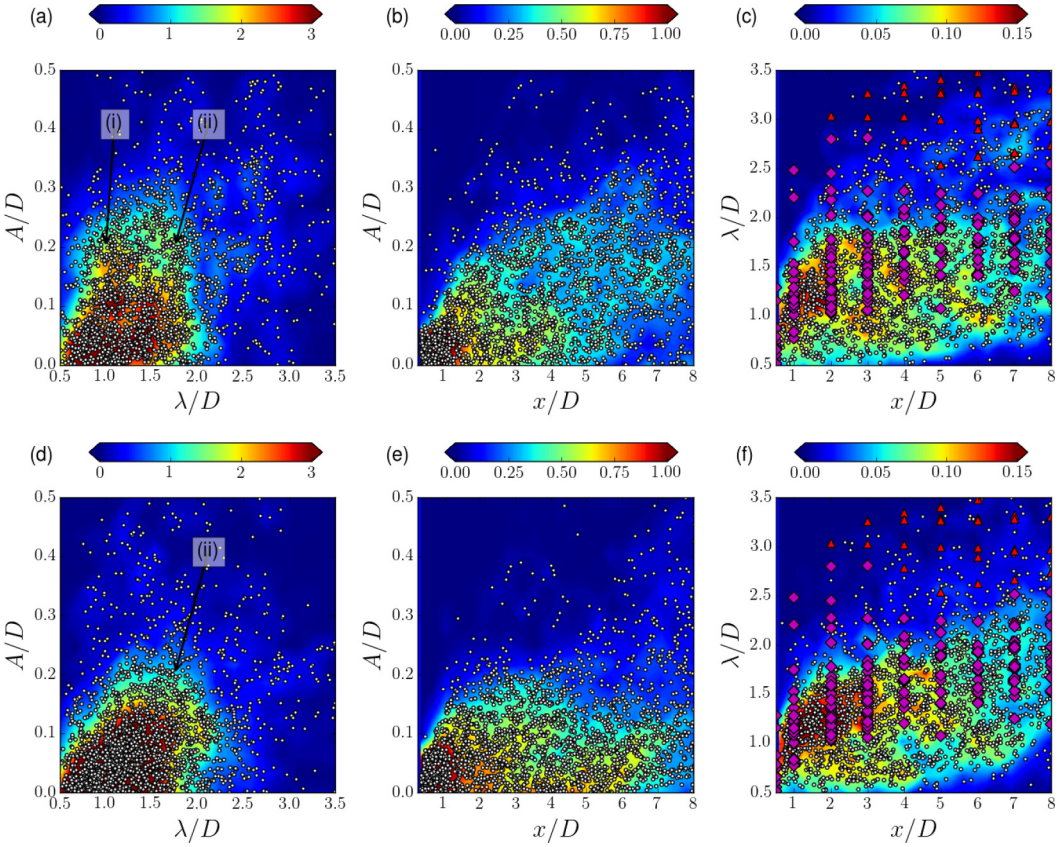

FIG. 11. Normalized joint probability function of the meander profiles: (a) and (d) wavelength λ/D and amplitude A/D, (b) and (e) amplitude A/D and axial distance x/D, and (c) and (f) wavelength λ/D and axial distance x/D. (a)–(c) are from data on the hub height plane $y = 0.8125D$ and (d)–(f) are from data on the normal center plane $z/D = 0$. The magenta diamond and red triangle markers in (c) and (f) are wavelengths of hub vortex frequencies and wake meandering frequencies, respectively, calculated from spectral data. The white dots are a sample of the data points.

D. Wake meandering characteristics

We now turn our attention to the behavior of the wake meandering profile, especially in the far wake, by computing statistics on all identified wake meander profiles. First, we focus on the wavelike characteristics of the meander profile, similarly to Howard *et al.* [6]. The pitch of the three-dimensional helical meander profile can be estimated as a wavelength of a two-dimensional wave, consistent with the two-dimensional meander signature shown in Fig. 8. To calculate both the amplitude and wavelength, the three-dimensional meander profile is projected on a two-dimensional plane. In the present analysis, two planes are chosen for the two-dimensional projection: the hub height plane parallel to the bottom wall [Figs. 11(a)–11(c)] and the center plane normal to the wall [Figs. 11(d)–11(f)]. From the projected two-dimensional plane, the wavelength is calculated as the distance between two consecutive maxima or minima. In this analysis, the minimum wavelength is $0.5D$ due to the spatial cutoff in the filtering process. The amplitude is the distance from one extremum to the centerline. The axial location of the wavelength is taken as the location of halfway between the extrema used to the calculate the wavelength. At this location, the amplitude is associated with the wavelength.

The wavelengths and amplitudes collected along the meander profile on the hub height parallel plane are compared in Fig. 11(a). The joint probability density function (JPDF) of the wavelength and the amplitude is similar to the results from Howard *et al.* [6] The highest densities of the joint probability occur in the region of $0.5 < \lambda/D < 1.5$ and $0 \sim A/D < 0.1$. The occurrence of high probability wavelengths near $1D$ indicates that the rotor diameter is a characteristic length scale of the meander. The probability of wavelengths shorter than $1D$ sharply drops off as these are filtered out. Two branches with high amplitude form in the space outside with regions of (a) low wavelength $1 < \lambda/D < 1.25$ and (b) higher wavelength $\lambda/D \sim 1.75$. These two branches can be understood by looking at Figs. 11(b) and 11(c) comparing, in separate plots, the amplitude and the wavelength as a function of the distance from the rotor. Branch (i) characterizes the region of $2 < x/D < 4$, between the near and far wakes. In this region of the wake, the rapidly expanding hub vortex coincides with the high amplitude of the meander. With low streamwise velocity due to the wake deficit, the wavelength remains small. Branch (ii) of the JPDF is largely due to long wavelengths present in the far wake $x/D > 5$ where wake meandering is creating the low-frequency motions captured by the meander profile. The high turbulence energy at the blade tip position, presented in Fig. 4 in the far wake, is manifested in the high amplitudes of large-scale meandering.

In both Figs. 11(b) and 11(c) the near and far wakes of the meander profile can be quantified by the evolution of the meander wavelength. In the near wake, both probability density functions of wavelength and amplitude remain concentrated on low values ($\lambda/D < 1.5$ and $A/D < 0.15$). The most probable region in the meander amplitude and wavelength domain is consistent with the hub vortex signature. With increasing distance to the rotor, the width of the JPDFs at each axial location is observed to increase, allowing for progressively larger, though still infrequent, oscillations. The highest probability of the wavelength remains, however, in the range $0.5 < \lambda/D < 2.0$. In the far wake, the amplitude is spread across the probability space in the range $0 \sim A/D < 0.5$ with an average near $A/D = 0.2$. The wavelength is in a large range $1 < \lambda/D < 3.5$ with higher probability densities around $\lambda/D = 1.5$ and $\lambda/D = 2.0$, denoting a marked increase in length scale, greater than $1D$, corresponding to large-scale wake meandering instability.

Similar wave behavior of the meandering profile occurs on the vertical plane shown in Figs. 11(d)–11(f). In Fig. 11(d), while the high probability region of low amplitude and wavelength exists because of the hub vortex, only branch (ii) is detectable in the JPDF. As discussed on the wall-parallel plane wave in Fig. 11(a), branch (i) represents the hub vortex expansion towards the tip vortices. On the vertical plane, this does not occur as rapidly, mainly due to the effect of the wall, which opposes the expansion of the wake meandering. In Fig. 11(e) the amplitude remains consistently $A/D < 0.2$ until after $x/D = 5$. Moreover, in comparison with the wall-parallel plane wave, the probability of high amplitude is always lower even in the far wake. Notwithstanding, the wavelength in both the parallel plane and vertical plane similarly grows with the downstream distance, indicating a dominant symmetry in the far wake meandering.

The wavelengths prevalent in the meandering profiles can be compared with the premultiplied power spectrum of the streamwise velocity in the low-frequency domain estimated in the wake of the turbine (see Fig. 12). The time series is chosen along the centerline plane at several radial locations including the hub height $y = H$, median blade location $y = H + D/4$, and the top-tip position $y = H + D/2$. Closest to the turbine at $x/D = 1$ in Fig. 12(a), there are several dominant frequencies. In the top-tip position the two higher-frequency peaks are the rotor frequency $\mathrm{St} = 1$ and the turbine blade frequency $\mathrm{St} = 3$, designated by the vertical dotted line. These frequency modes are observed to be highly energized near the rotor plane but dissipate quickly downstream (by $x/D = 5$ they are indistinguishable). From $1 < x/D < 3$, a range of lower frequencies is represented with energetic contributions corresponding to $\mathrm{St} = fD/U_{\mathrm{hub}} = 0.35 - 0.6$ with peak power at $\mathrm{St} = 0.45$. This contribution is only associated with locations $H < y \leqslant H + D/4$, indicating that it is not yet accounting for the tip vortex dynamics. This range indeed corresponds to the hub vortex Strouhal number consistent with several studies [6,19,40]. Focusing on the hub vortex frequency range, in Fig. 12(a) the power is maximum at $y = H + D/10$. In consecutive figures, from Figs. 12(a) to 12(c), the peak power level gradually decreases closer to the centerline, while an increase in power

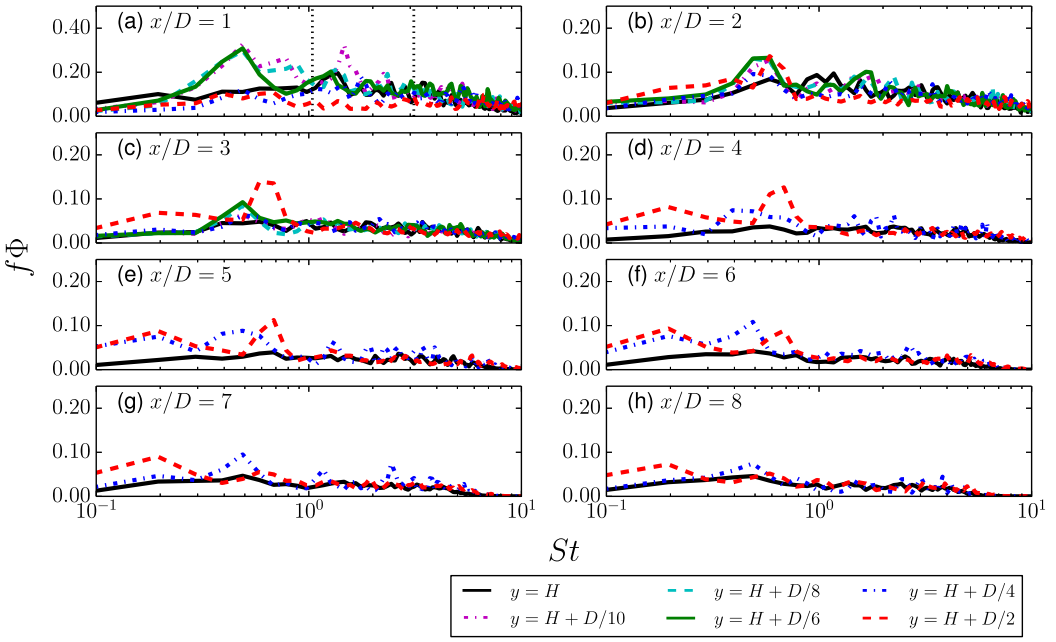

FIG. 12. Premultiplied power density spectrum $f\Phi$ of the velocity magnitude $|u|$ on the plane $z/D = 0$ at several vertical locations at downstream locations (a) $x/D = 1$, (b) $x/D = 2$, (c) $x/D = 3$, (d) $x/D = 4$, (e) $x/D = 5$, (f) $x/D = 6$, (g) $x/D = 7$, and (h) $x/D = 8$. The vertical dotted lines in (a) are the St based on the rotor and blade passing frequencies.

is witnessed farther from the centerline, indicating that the hub vortex quickly expands towards the tip shear layer. From Figs. 12(d) to 12(h) the energy level of the hub vortex frequency range present at $y = H + D/4$ slowly dissipates but is persistent throughout the entire domain. The persistence of the hub vortex frequencies far downstream implies that the hub vortex affects the flow field in the far field as observed in the streamwise vorticity contours in Fig. 5.

Starting at $x/D = 3$ and continuing to far downstream locations [Figs. 12(c)–12(h)], another energetic low-frequency range appears around the tip heights, corresponding to St = 0.15–0.3, thus at lower frequencies as compared to the hub vortex frequencies. Gradually, the $y = H + D/4$ location also manifests energy is this frequency range, starting with $x/D = 4$. This signal is recognized as the signature of wake meandering, which has been observed to peak at St = 0.23 [4] and at St = 0.28 [8] at $x/D = 5$. Medici and Alfredsson [7] measured a range of St = 0.15–0.25, very close to the range of frequencies highlighted here. In our study the peak wake meandering frequency occurs for St = 0.15 at $x/D = 5$ in the top-tip position and at $y = H + D/4$. It is not coincidental that the probability of high amplitudes and long wavelengths of the meander profile begins to occur around this downstream location ($x/D = 5$) where the turbulence kinetic energy in the top-tip position has a marked increase (see Fig. 4).

In order to directly compare the wavelengths of the meander profile to the spectral data, Taylor's hypothesis is used to obtain a wavelength range of the hub vortex and wake meandering from the spectrum peak frequencies. Using the local mean velocity, key energetic spectral wavelengths $\lambda/D = U/U_{\text{hub}}/\text{St}$ are computed from the frequencies corresponding to the hub vortex and wake meandering. The reconstructed wavelengths of the hub vortex frequency peaks are shown as the magenta diamond markers in Figs. 11(c) and 11(f). A majority of the markers from spectral data follow the contours of high probability in the JPDF from $x/D = 1$ to $x/D = 8$ with a few at higher wavelengths but still correlating well with the JPDF. Similarly, the wake meandering reconstructed wavelengths are plotted in the same figures. Here the low frequencies $0.15 < \text{St} < 0.3$ correspond to

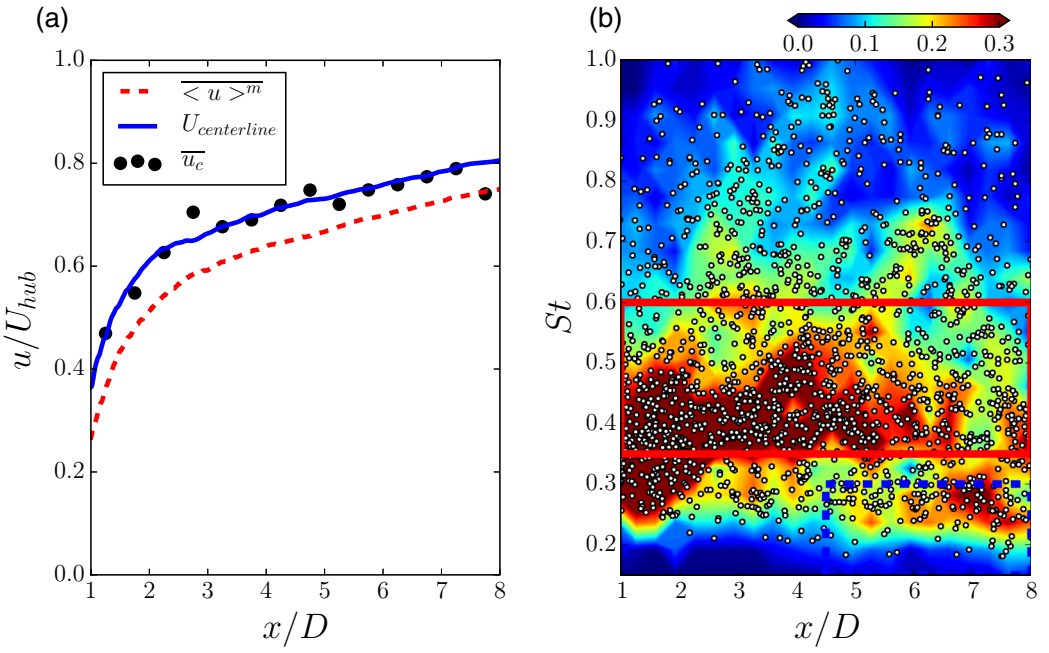

FIG. 13. (a) Mean meander streamwise convection velocity $\overline{u_c}$ compared with the mean centerline velocity $U_{\text{centerline}}$ and average large-scale streamwise velocity along the meander $\overline{\langle u \rangle^m}$. (b) The JPDF of St and x/D. The red boxed area $0.35 < \text{St} < 0.6$ and blue dashed box region $0.15 < \text{St} < 0.3$ are defined by the range of the hub vortex and wake meandering spectral signature, respectively, as obtained by spectral analysis (see Fig. 12).

large wavelengths $\lambda/D = 3.0$–4.0, which is consistent with a large range of wavelengths $1 < \lambda/D < 3.5$ obtained from the meandering profile. The low wavelength is only present in the far wake and is the signature of wake meandering in the meander profile. The short wavelengths in the far wake can be attributed to the remains of the higher-frequency hub vortex signature still present in the wake.

A mean convection velocity with respect to the downstream distance of the meander profile is obtained through averaging the instantaneous wave speed of the meander profile. The wave convection velocity is calculated by tracking the distance the meander profile extrema travel between successive time instances. Figure 13(a) plots the calculated average mean convection velocity of the meander profile $\overline{u_c}$ with the mean centerline streamwise velocity $U_{\text{centerline}}$ and the average large-scale streamwise velocity along the meander $\overline{\langle u \rangle^m}$. All three velocities increase with the recovering wake, quickly recovering in the near wake and then slowly farther downstream. The large-scale streamwise velocity along the meander is always less than the centerline velocity because the meander profile is defined along the velocity minimum at each position. The meander wake convection velocity falls in between the range of the centerline velocity and the large-scale streamwise along the meander. From these results, we can reasonably assume that the meandering wake convects downstream with the local streamwise velocity and the increase in wavelength downstream can be caused in part by the wake recovery. In other words, the wake meander is stretched along the streamwise direction.

Using the mean convection velocity of the meander profile and the reconstructed wavelengths calculated from the meander profiles, reconstructed frequencies (St) of the meander profile are calculated with the $\text{St} = fD/U_{\text{hub}} = (\overline{u_c}/U_{\text{hub}})/(\lambda/D)$ and are shown in the JPDF in Fig. 13(b). The highest probability of the reconstructed St is in the range $0.4 < \text{St} < 0.5$ for all downstream distances that correspond well to the peak hub vortex frequency signals ($0.35 < \text{St} < 0.6$) from the power spectrum from Fig. 12, designated by the red box in Fig. 13(b). The hub vortex energy contributions first appear immediately downstream of the turbine and persist downstream; the frequencies from the reconstructed meander frequencies also persist into the far wake. The probability of the hub vortex

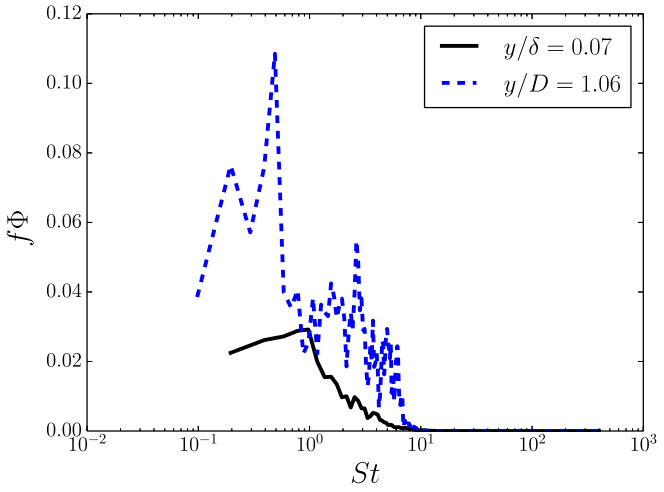

FIG. 14. Premultiplied power density spectrum of time series in the logarithmic layer ($y/\delta = 0.06$) of the incoming boundary layer (solid line) and in the turbine wake ($x/D = 5$) at $y/D = 1.06$ (dashed line).

frequencies from the meander profile detection technique in the far wake begin to diminish similar to the corresponding energetic contribution from the power spectrum. The wake meandering frequency range [$0.15 < \mathrm{St} < 0.3$, marked by the blue box on Fig. 13(b)] is present only in the far wake ($x/D > 4$), as expected. Both the frequency range from the power spectrum and the reconstructed frequencies of the meander profile for wake meandering correlate well. The probability of the wake meandering frequencies persists through the end of the domain analyzed and the meander profile technique can only capture a few wavelengths of wake meandering. Also, we would like to remind the reader that the energetic contributions of the wake meandering frequencies are much higher than those from the hub vortex frequencies.

The effect of the turbulent boundary layer height on the development of the turbine wake has not been addressed here; however, we acknowledge that the largest and most energetic turbulent structures, statistically populating the logarithmic layer, could interact with the wake structure, favoring entrainment of high momentum fluids into the wake and destabilizing the tip vortex structure. Such interaction depends on the location of the rotor with respect to the vertical extent of the wall region. In order to study realistic conditions, the model turbine has a hub to boundary layer height ratio of about 18%, which is comparable to the utility scale turbine in a near-neutral atmospheric boundary layer, in flat regions. Consequently, also the mean shear across the turbine rotor is overall comparable, though in specific synoptic conditions a slight increase of mean shear at the utility scale is observed as compared to the wind tunnel scale [41].

Further effects on the turbine wake can clearly been seen as the rapid breakdown of the tip vortices and entrainment of high momentum fluid into the turbine wake through the annular shear layer developing around the rotor. Incoming boundary layer turbulence at the large scale is expected to perturb and partially disrupt the tip vortex system favoring shear instabilities. This can only promote interaction with the tip vortex. Therefore, wake meandering is expected to be amplified under incoming coherent boundary layer turbulence. This undoubtedly is one of the major causes for the quick transition from the near wake to the far wake, marked by the large-scale periodic wake meandering motions [6,20]. Numerous studies [14,18,42] have shown the effect of the turbines in the uniform inflow or otherwise ideal inflow. They show significant coherence many diameters downstream of the rotor as tip vortices convect and wake deficit recovers. Nonetheless, they observe an eventual breakdown of the tip vortices and hub vortex, evolving into large-scale meandering flows. As for the present work, Fig. 14 shows a premultiplied power spectrum of (i) the inflow turbulent

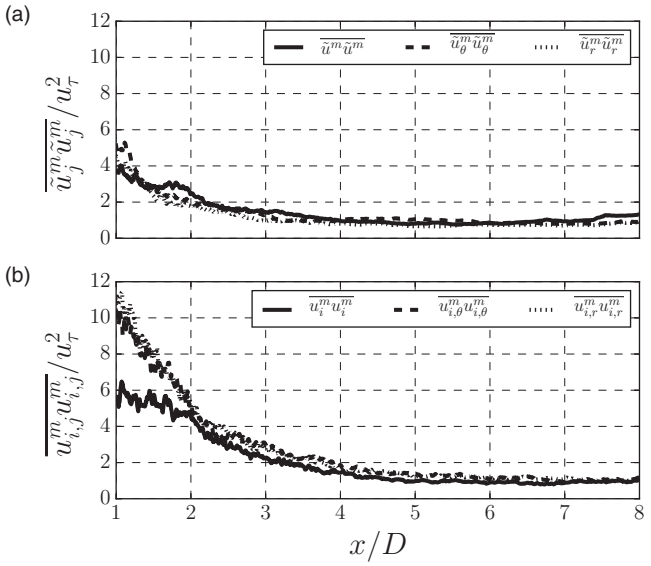

FIG. 15. (a) Coherent velocity variance $\overline{\tilde{u_j}^m \tilde{u_j}^m}/u_*^2$ along the meander. (b) Incoherent velocity variance $\overline{u_{i,j}^m u_{i,j}^m}/u_*^2$ along the meander.

boundary layer in the logarithmic region $y/\delta = 0.07$, where δ is the boundary layer height, outside the influence of the wake and (ii) the downstream wake at $x/D = 5$ at $y/D = 1.06$. The locations are chosen where large coherent structures are expected to be most prominent in both the turbulent boundary layer and turbine wake, respectively. The first two low-frequency peaks of the downstream wake spectrum are the wake meandering and hub vortex frequency, respectively, and are clearly the most energetic frequencies present in the wake. Moreover, these frequencies are not distinguished in the power spectrum of the incoming, undisturbed flow. This implies that the energetic frequency modes associated with the large-scale structures present in the boundary layer are not related to the wake meandering or hub vortex frequencies, even though interactions are possible.

E. Wake meandering turbulence

The turbulence kinetic energy in wake meandering is due to both coherent and incoherent fluctuations. The coherent turbulence velocity along the meander profile is from the coherent hub vortex wake and meandering motions in the wake of the turbine. To investigate the turbulence level in the wake, the mean of the squared coherent and incoherent velocities, the coherent and incoherent velocity variances, respectively, along the meander profile are computed conditioned on the distance to the turbine. These turbulence velocity variances are normalized by the shear velocity squared u_τ^2 of the inflow boundary layer. The turbulence in the wake is shown to be much larger that the inflow turbulence as the turbine motion generates high levels of turbulence. The coherent velocity variance is shown in Fig. 15(a). All three components of the coherent velocity peak nearest the turbine and are similar in magnitude, indicating that the coherent turbulence in the near wake is fairly isotropic. The coherent velocity variance decreases further downstream uniformly. Around $z/D = 4$ the azimuthal coherent velocity variance increases compared to the other components and peaks at $x/D = 5$. This position coincides with previous evidence of the high level of turbulence kinetic energy at the same distance in Fig. 4 and previous suggestions that this is the position of wake meandering emergence in the wake. Furthermore, spectral analysis confirms that the peak energy near the wake meandering frequency and growth of large amplitude and wavelengths of the meander profile occur around $x/D = 5$. Consequently, we infer that large-scale azimuthal turbulence fluctuations have a large

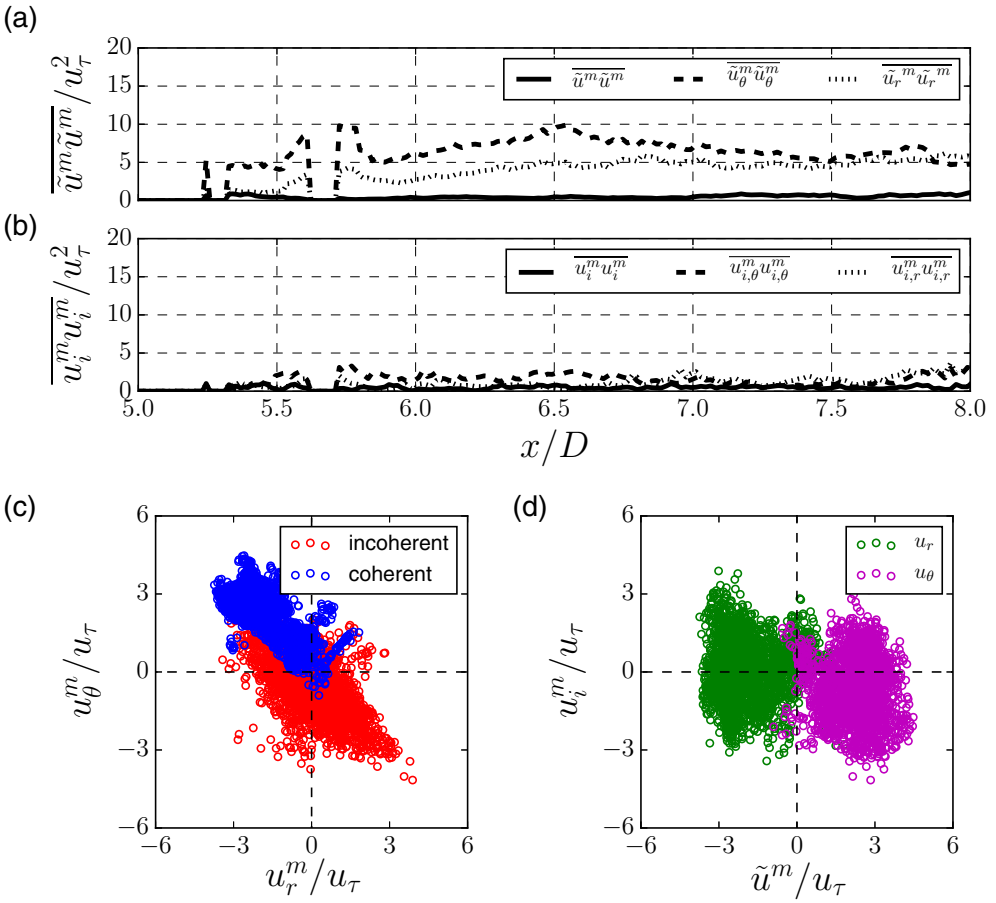

FIG. 16. (a) Conditional coherent velocity variance $\overline{\tilde{u_j}^m\tilde{u_j}^m}/u_*^2$ along the meander in the far wake $x/D > 5$ and $r/D > 0.5$. (b) Conditional incoherent velocity variance $\overline{u_{i,j}^m u_{i,j}^m}/u_*^2$ along the meander in the far wake $x/D > 5$ and $r/D > 0.5$. (c) Coherent (blue) and incoherent (red) radial velocity vs azimuthal velocity in the far wake $x/D > 5$ and $r/D > 0.5$. (d) Radial (green) and azimuthal (magenta) coherent velocity vs incoherent velocity in the far wake $x/D > 5$ and $r/D > 0.5$.

contribution to the energy in wake meandering. Further downstream, the contribution of azimuthal fluctuations decreases to be nearly equal to the other components.

The incoherent turbulence energy also contributes to the total turbulence energy in the flow. As with the coherent velocity variance, the peak incoherent velocity variance is in the near wake at $x/D = 1$ as shown in Fig. 15(b). Unlike the coherent turbulent velocity, where all components of the velocity variance peak near the same value, the peak velocity variance is not isotropic as the axial component is significantly lower than the other components. Moreover, all components of the incoherent turbulence are larger than the coherent velocity variance, suggesting that the vortex shedding over the nacelle and the hub vortex sustains incoherent turbulent fluctuations. At $x/D > 5$, the incoherent velocity variance remains nearly constant for all three components and is comparable in magnitude to the coherent velocity variance. However, there is no footprint in the incoherent turbulence of wake meandering in the far wake. It appears that wake meandering is influenced by coherent structures but has a high level of incoherent turbulence. The influence of the coherent turbulence on the meander profile, especially in the far wake, is another indication that the meander profile captures the coherent motions of wake meandering.

In order to elucidate the turbulence levels that are occurring near the tip position where it is expected for wake meandering to be most prevalent, the coherent and incoherent velocity variances along the meander profile are limited to the outer rotor region ($r/D > 0.5$). This operation removes data where the meander profile is away from the tip vortices. Figure 16(a) shows the conditional coherent velocity variance. All variances prior to $x/D = 5.5$ are zero because the meander profile does not expand to $r/D = 0.5$ until after that axial position. However, compared to the coherent velocity variance in Fig. 15(a), the conditional variance is several times larger. The azimuthal velocity variance is the largest of the three components, verifying once again that the azimuthal coherent velocity fluctuations due to the previously discussed precession of the hub vortex are dominant contributors to wake meandering. There is also a significant level of radial velocity variance, while the streamwise velocity variance remains low, indicating that the turbulence kinetic energy in the tip position is mainly affected by coherent fluctuations in the azimuthal and radial directions. The conditional incoherent velocity variance shown in Fig. 16(b) has a much lower magnitude than the coherent turbulence in the same area of the wake. Further investigation of the relationship of the radial velocity and the azimuthal velocity in Fig. 16(c) reveals that the scatter of the coherent velocities almost solely resides in the quadrant where azimuthal velocity is positive and radial velocity is negative. Consequently, this indicates that wake meandering has coherent rotational motion in the opposite direction of the turbine rotation. Considering previous results discussed with Fig. 9, while the mean azimuthal velocity is negligible, coherent fluctuations of wake meandering are the primary cause of the rotation in the far wake. Moreover, with a negative coherent radial velocity, the wake is entraining fluid from outside. The incoherent azimuthal and radial velocity scatter indicates incoherent fluctuations occurring in all four quadrants but with clear tails in both positive azimuthal or negative radial components and negative azimuthal or positive radial components. Figure 16(d) shows the correlation with the coherent and incoherent fluctuations of both the azimuthal and radial velocity components. While the coherent azimuthal velocity is always positive, the incoherent azimuthal velocity does not appear to be well correlated. Similarly, the incoherent radial velocity does not correlate well with the coherent radial velocity.

V. CONCLUSION

The nature of the wake behind a wind turbine is complex and highly three dimensional and is dominated by the precession fluctuations of a large helical structure. To investigate the coherent structures in the wake, a numerical study using LES and the curvilinear immersed boundary method to resolve the geometrical details of a miniature turbine in a wind tunnel was performed. The near wake region is dominated by the counterrotating low-frequency hub vortex formed behind the nacelle in an inner wake separate from the corotating tip vortices and is marked by the low amplitude and short wavelength of the meander profile. The hub vortex in the immediate vicinity of the turbine nacelle is comprised of a toroidal recirculation zone and exhibits large-scale slowly precessing motions in the direction opposite to the turbine rotation, very much resembling spiral vortex breakdown. The hub vortex entrains fluid and expands radially with downstream distance until it starts interacting with the tip vortices. The interaction of the inner and outer wakes culminates in a high turbulence region in the far wake, so-called wake meandering, which manifests as low-frequency, long-wavelength coherent structures.

Expanding on a filtering technique from Howard *et al.* [6] for tracking the instantaneous wake meandering, both temporal and spatial data from LES were used to capture the meandering location, reconstruct the three-dimensional meander profiles, and decompose the flow field into mean, coherent, and incoherent components. The meander profile allows us to investigate the coherent structures in the near wake and the far wake. By tracking the hub vortex, the meander profile shows that the rotational momentum of the hub vortex persists into the far wake where the coherent structures maintain an instantaneous counterrotation. The wavelengths of the meander profiles show that where the hub vortex intercepts the tip shear layer, longer wavelengths form coinciding with the onset of wake meandering. Confirmed by spectral analysis, both wavelengths of the hub vortex

and wake meandering are present at least eight diameters downstream. Using the meander profiles, conditional averages at the tip positions in the wake reveal high levels of coherent azimuthal and radial turbulence compared to the low intensity of the incoherent turbulence. This allows us to conclude that the region of high turbulent kinetic energy along the top-tip position, marking the onset of wake meandering, is influenced by coherent turbulence mainly in the azimuthal direction. Furthermore, the directions of the coherent azimuthal fluctuations are counterrotating, demonstrating the persistence of the hub vortex in the far wake.

Our results provide additional evidence in support of the computational work of Kang *et al.* [20], who were the first to demonstrate the large-scale instability of the hub vortex and its impact on the intensity of far wake meandering. Kang *et al.* [20] employed an axial flow hydrokinetic turbine with a fairly bulky nacelle; the ratio of the nacelle to rotor diameter in Ref. [20] was equal to 0.16. The results we report herein, however, show that the same large-scale instability of the hub vortex occurs in the wake of an entirely different turbine design, a miniature wind turbine with a considerably smaller nacelle (the ratio of the nacelle to rotor diameter is equal to 0.1). Therefore, our work, in conjunction with the previous studies by Kang *et al.* [20] and Howard *et al.* [6] as well as the experimental and computational studies of Iungo *et al.* [19], points to the conclusion that the large-scale spiral instability of the hub vortex and impact on far wake meandering are phenomena that could be ubiquitous in wind turbine wakes. Additional work is needed to study whether such rich large-scale dynamics also characterize the wakes of utility scale wind turbines.

ACKNOWLEDGMENTS

This work was supported by the US Department of Energy (Grants No. DE-EE0002980, No. DE-EE0005482, and No. DE-AC04-94AL85000) and Sandia National Laboratories. Computational resources were provided by Sandia National Laboratories and the University of Minnesota Supercomputing Institute.

[1] D. Medici and P. H. Alfredsson, Measurements on a wind turbine wake: 3D effects and bluff body vortex shedding, Wind Energy **9**, 219 (2006).

[2] S. J. Andersen, J. N. Sørensen, and R. Mikkelsen, Simulation of the inherent turbulence and wake interaction inside an infinitely long row of wind turbines, J. Turbul. **14**, 1 (2013).

[3] C. VerHulst and C. Meneveau, Large eddy simulation study of the kinetic energy entrainment by energetic turbulent flow structures in large wind farms, Phys. Fluids **26**, 025113 (2014).

[4] V. L. Okulov and J. N. Sørensen, Stability of helical tip vortices in a rotor far wake, J. Fluid Mech. **576**, 1 (2007).

[5] S. Ivanell, R. Mikkelsen, J. N. Sørensen, and D. Henningson, Stability analysis of the tip vortices of a wind turbine, Wind Energy **13**, 705 (2010).

[6] K. B. Howard, A. Singh, F. Sotiropoulos, and M. Guala, On the statistics of wind turbine wake meandering: An experimental investigation, Phys. Fluids **27**, 075103 (2015).

[7] D. Medici and P. H. Alfredsson, Measurements behind model wind turbines: Further evidence of wake meandering, Wind Energy **11**, 211 (2008).

[8] L. P. Chamorro, C. Hill, S. Morton, C. Ellis, R. E. A. Arndt, and F. Sotiropoulos, On the interaction between a turbulent open channel flow and an axial-flow turbine, J. Fluid Mech. **716**, 658 (2013).

[9] V. L. Okulov, I. V. Naumov, R. F. Mikkelsen, I. K. Kabardin, and J. N. Sørensen, A regular Strouhal number for large-scale instability in the far wake of a rotor, J. Fluid Mech. **747**, 369 (2014).

[10] L. P. Chamorro and F. Porté-Agel, A wind-tunnel investigation of wind-turbine wakes: Boundary-layer turbulence effects, Bound.-Lay. Meteorol. **132**, 129 (2009).

[11] H. Hu, Z. Yang, and P. Sarkar, Dynamic wind loads and wake characteristics of a wind turbine model in an atmospheric boundary layer wind, Exp. Fluids **52**, 1277 (2012).

[12] J. Hong, M. Toloui, L. P. Chamorro, M. Guala, K. Howard, S. Riley, J. Tucker, and F. Sotiropoulos, Natural snowfall reveals large-scale flow structures in the wake of a 2.5-MW wind turbine, Nat. Commun. **5**, 4216 (2014).
[13] S. Ivanell, J. N. Sørensen, R. Mikkelsen, and D. Henningson, Analysis of numerically generated wake structures, Wind Energy **12**, 63 (2009).
[14] N. Troldborg, J. N. Sorensen, and R. Mikkelsen, Numerical simulations of wake characteristics of a wind turbine in uniform inflow, Wind Energy **13**, 86 (2010).
[15] S. E. Widnall, The stability of a helical vortex filament, J. Fluid Mech. **54**, 641 (1972).
[16] B. P. Gupta and R. G. Loewy, Theoretical analysis of the aerodynamic stability of multiple, interdigitated helical vortices, AIAA J. **12**, 1381 (1974).
[17] H. Levy and A. G. Forsdyke, The steady motion and stability of a helical vortex, Proc. R. Soc. London Ser. A **120**, 670 (1928).
[18] M. Felli, R. Camussi, and F. Di Felice, Mechanisms of evolution of the propeller wake in the transition and far fields, J. Fluid Mech. **682**, 5 (2011).
[19] G. V. Iungo, F. Viola, S. Camarri, F. Porté-Agel, and F. Gallaire, Linear stability analysis of wind turbine wakes performed on wind tunnel measurements, J. Fluid Mech. **737**, 499 (2013).
[20] S. Kang, X. Yang, and F. Sotiropoulos, On the onset of wake meandering for an axial flow turbine in a turbulent open channel flow, J. Fluid Mech. **744**, 376 (2014).
[21] G. C. Larsen, H. A. Madsen, K. Thomsen, and T. J. Larsen, Wake meandering: A pragmatic approach, Wind energy **11**, 377 (2008).
[22] K. B. Howard, J. S. Hu, L. P. Chamorro, and M. Guala, Characterizing the response of a wind turbine model under complex inflow conditions, Wind Energy **18**, 729 (2014).
[23] S. Kang, I. Borazjani, J. A. Colby, and F. Sotiropoulos, Numerical simulation of 3D flow past a real-life marine hydrokinetic turbine, Adv. Water Resour. **39**, 33 (2012).
[24] S. Kang and F. Sotiropoulos, Numerical modeling of 3D turbulent free surface flow in natural waterways, Adv. Water Resour. **40**, 23 (2012).
[25] S. Kang, A. Lightbody, C. Hill, and F. Sotiropoulos, High-resolution numerical simulation of turbulence in natural waterways, Adv. Water Resour. **34**, 98 (2011).
[26] A. Khosronejad, S. Kang, and F. Sotiropoulos, Experimental and computational investigation of local scour around bridge piers, Adv. Water Resour. **37**, 73 (2012).
[27] L. Ge and F. Sotiropoulos, A numerical method for solving the 3D unsteady incompressible Navier-Stokes equations in curvilinear domains with complex immersed boundaries, J. Comput. Phys. **225**, 1782 (2007).
[28] A. Gilmanov and F. Sotiropoulos, A hybrid Cartesian/immersed boundary method for simulating flows with 3D, geometrically complex, moving bodies, J. Comput. Phys. **207**, 457 (2005).
[29] J. Smagorinsky, General circulation experiments with the primitive equations: I. The basic experiment*, Mon. Weather Rev. **91**, 99 (1963).
[30] M. Germano, U. Piomelli, P. Moin, and W. H. Cabot, A dynamic subgrid-scale eddy viscosity model, Phys. Fluids A **3**, 1760 (1991).
[31] X. Yang, F. Sotiropoulos, R. J. Conzemius, J. N. Wachtler, and M. B. Strong, Large-eddy simulation of turbulent flow past wind turbines/farms: The virtual wind simulator (VWIS), Wind Energy **18**, 2025 (2015).
[32] A. Gilmanov, T. B. Le, and F. Sotiropoulos, A numerical approach for simulating fluid structure interaction of flexible thin shells undergoing arbitrarily large deformations in complex domains, J. Comput. Phys. **300**, 814 (2015).
[33] N. E. Joukowski, Vortex theory of a rowing screw, Tr. Otd. Fiz. Nauk Ova. Lubit. Estestvozn. **16**, 1 (1912).
[34] A. K. M. Hussain, Coherent structures and turbulence, J. Fluid Mech. **173**, 303 (1986).
[35] A. Chrisohoides and F. Sotiropoulos, Experimental visualization of Lagrangian coherent structures in aperiodic flows, Phys. Fluids **15**, L25 (2003).
[36] S. Leibovich, The structure of vortex breakdown, Annu. Rev. Fluid Mech. **10**, 221 (1978).
[37] T. Sarpkaya, On stationary and traveling vortex breakdowns, J. Fluid Mech. **45**, 545 (1971).
[38] M. Felli, F. Di Felice, G. Guj, and R. Camussi, Analysis of the propeller wake evolution by pressure and velocity phase measurements, Exp. Fluids **41**, 441 (2006).

[39] R. Muscari, A. Di Mascio, and R. Verzicco, Modeling of vortex dynamics in the wake of a marine propeller, Comput. Fluids **73**, 65 (2013).

[40] F. Viola, G. V. Iungo, S. Camarri, F. Porté-Agel, and F. Gallaire, Prediction of the hub vortex instability in a wind turbine wake: Stability analysis with eddy-viscosity models calibrated on wind tunnel data, J. Fluid Mech. **750**, R1 (2014).

[41] K. B. Howard and M. Guala, Upwind preview to a horizontal axis wind turbine: A wind tunnel and field-scale study, Wind Energy **19**, 1371 (2015).

[42] M. Sherry, A. Nemes, D. L. Jacono, H. M. Blackburn, and J. Sheridan, The interaction of helical tip and root vortices in a wind turbine wake, Phys. Fluids **25**, 117102 (2013).